

---

This is the **submitted version** of the journal article:

Yang, Dawei; Liang, Zhifu; Tang, PengYi; [et al.]. «A High conductivity 1D -d conjugated metal-organic framework with efficient polysulfide trapping-diffusion-catalysis in lithium-sulfur batteries». Advanced materials, Vol. 34, issue 10 (March 2022), art. 2108835. DOI 10.1002/adma.202108835

---

This version is available at <https://ddd.uab.cat/record/271941>

under the terms of the  <sup>IN</sup>  
COPYRIGHT license

# A High Conductivity One-Dimensional $\pi$ -d Conjugated Metal-Organic Framework with Efficient Polysulfide Trapping-Diffusion-Catalysis in Lithium-Sulfur Batteries

Dawei Yang<sup>+</sup>, Zhifu Liang<sup>+</sup>, Pengyi Tang<sup>+</sup>, Chaoqi Zhang, Mingxue Tang, Qizhen Li, Jordi Jacas Biendicho, Junshan Li, Marc Heggen, Rafal E. Dunin-Borkowski, Ming Xu\*, Jordi Llorca, Jordi Arbiol\*, Joan Ramon Morante, Shu-Lei Chou\*, Andreu Cabot\*

*D. W. Yang, Z. F. Liang, C. Q. Zhang, Dr. J. J. Biendicho, Prof. J. R. Morante, Prof. A. Cabot  
Catalonia Institute for Energy Research - IREC,  
Sant Adrià de Besòs, Barcelona, 08930, Spain  
Email: [acabot@irec.cat](mailto:acabot@irec.cat)*

*D. W. Yang, C. Q. Zhang, Prof. J. R. Morante  
Department of Electronic and Biomedical Engineering  
Universitat de Barcelona, 08028 Barcelona, Spain*

*Z. F. Liang, Prof. J. Arbiol  
Catalan Institute of Nanoscience and Nanotechnology (ICN2)  
CSIC and BIST, Campus UAB, Bellaterra, 08193 Barcelona, Spain  
Email: [arbiol@icrea.cat](mailto:arbiol@icrea.cat)*

*Dr. P. Y Tang, Dr. M Heggen, Prof. R E. Dunin-Borkowski  
Ernst Ruska-Centre for Microscopy and Spectroscopy with Electrons and Peter Grünberg  
Institute Forschungszentrum Jülich GmbH 52425 Jülich, Germany*

*Dr. P. Y Tang  
State Key Laboratory of Information Functional Materials, 2020 X-Lab, Shanghai Institute of  
Microsystem and Information Technology, Chinese Academy of Sciences, Shanghai, P. R. China*

*Prof. M. X. Tang  
Center for High Pressure Science and Technology Advanced Research, Beijing 100094, China*

*Q. Z. Li  
Department of Biomedical Engineering, Southern University of Science and Technology (SUSTech),  
Shenzhen, Guangdong, 518055, China*

*Dr. J. S. Li*

*Institute of Fundamental and Frontier Science, University of Electronic Science and Technology of China, 610054, Chengdu, China*

*Prof. J. Llorca*

*Institute of Energy Technologies, Department of Chemical Engineering and Barcelona Research Center in Multiscale Science and Engineering, Universitat Politècnica de Catalunya, EEBE, 08019, Barcelona, Spain*

*Prof. M. Xu*

*State Key Laboratory of Chemical Resource Engineering, Beijing University of Chemical Technology, Beijing 100029, P. R. China*

*Email: [mingxu@mail.buct.edu.cn](mailto:mingxu@mail.buct.edu.cn)*

*Prof. S. L. Chou*

*Institute for Carbon Neutralization, College of Chemistry and Materials Engineering, Wenzhou University, Wenzhou, Zhejiang 325035, China*

*E-mail: [chou@wzu.edu.cn](mailto:chou@wzu.edu.cn)*

*Prof. J. Arbiol, Prof. A. Cabot*

*ICREA*

*Pg. Lluís Companys 23, 08010 Barcelona, Spain*

+ These authors contributed equally to this work

Keywords: metal organic framework, lithium polysulfide,  $\pi$ -d conjugation, lithium-sulfur battery

# Abstract

Lithium-sulfur batteries (LSBs) offer notable advantages over conventional lithium ion batteries, but their implementation is limited by the sluggish conversion kinetics of lithium polysulfides (LiPS), the dissolution and diffusion of LiPS, and the poor electrical conductivity of sulfur and lithium sulfide. Herein, we present a one-dimensional (1D)  $\pi$ -d conjugated metal-organic framework, Ni-MOF-1D, as an efficient sulfur host to overcome these limitations. Experimental results and density functional theory (DFT) calculations demonstrate that Ni-MOF-1D is characterized by a remarkable binding strength for trapping soluble LiPS species. Ni-MOF-1D also acts as an effective catalyst for S reduction during the discharge process and  $\text{Li}_2\text{S}$  oxidation during the charge process. In addition, the delocalization of electrons in the  $\pi$ -d system of Ni-MOF-1D provides a superior electrical conductivity to improve electron transfer. Thus, cathodes based on Ni-MOF-1D enable LSBs with excellent performance, including a remarkable initial capacity of  $1491 \text{ mA h g}^{-1}$ , superior rate performance of  $575 \text{ mAh g}^{-1}$  at 8 C, impressive cycling stability with over 82% capacity retention over 1000 cycles at 3 C, and a high areal capacity of  $5.36 \text{ mAh cm}^{-2}$  under a high sulfur loading of  $4.3 \text{ mg cm}^{-2}$ . While this work particularly focuses on the synthesis and performance of a Ni-based MOF, the strategies and advantages here demonstrated can be extended to a broader range of  $\pi$ -d conjugated MOFs materials, which we believe have a high potential as sulfur host in LSBs.

# Introduction

Lithium-sulfur batteries (LSBs) have attracted extensive interest as the next generation of energy storage systems due to the ultra-high theoretical capacity of sulfur ( $1672 \text{ mAh g}^{-1}$ ), their high theoretical energy density ( $2600 \text{ W h kg}^{-1}$ ), low cost and potential for low environmental impact.<sup>1-3</sup> However, their commercial application is delayed by several unsolved challenges, including: i) the electrically insulating nature of sulfur and its sluggish redox reaction requiring a high polarization;<sup>4,5</sup> ii) the solubility of lithium polysulfides (LiPS) in the liquid electrolyte and its diffusion and deposition on the lithium anode, which lead to a severe capacity decline and a low coulombic efficiency;<sup>6,7</sup> iii) the huge cathode volume change (up to 80%) during operation that may lead to significant structural degradations.<sup>8</sup>

Owing to the enormous potential socio-economic impact of LSBs, intense efforts are being dedicated to solving their limitations. The most extended strategy is to incorporate a high surface area carbonaceous sulfur host on the cathode to provide the required high electrical conductivity, retain LiPS and confine the volume expansion. However, while several carbon-based materials, including graphene, carbon nanotubes and hollow carbon spheres, have been employed as sulfur host in LSB cathodes,<sup>9-12</sup> the physical retention of LiPS by carbon meso-/micropores has limited effectiveness due to the weak van der Waals interaction between the nonpolar surface of carbon and the polar LiPS.<sup>13</sup> To promote this interaction, the incorporation of additional inorganic compounds, e.g. transition-metal oxides,<sup>14</sup> nitrides,<sup>15</sup> and sulfides,<sup>16</sup> with strong dipole-dipole interaction with LiPS, have been proved effective to inhibit the LiPS shuttle effect.<sup>17</sup> As drawbacks, most of these polar hosts suffer from a relatively poor electrical conductivity, moderate density of adsorption sites, and relatively high weight, which result in a poor rate performance and modest specific and gravimetric capacities.<sup>18</sup>

Metal-organic frameworks (MOFs) with a very large density of LiPS adsorption sites have a huge potential as sulfur host.<sup>19,20</sup> The Lewis acid-base interactions between MOFs and LiPS have been demonstrated to effectively restrain the migration of LiPS, thus improving the LSB performance.<sup>21,22</sup> Besides, their large structural and chemical diversity provide numerous degrees of freedom to optimize their performance. Nevertheless, most MOFs are electrical insulators. Thus, to be applied as cathode material in LSBs, MOFs are typically combined with

additional conductive materials or are carbonized through annealing at high temperatures.<sup>22</sup> Alternatively,  $\pi$ -d conjugated MOFs, which are similar to  $\pi$ - $\pi$  conjugated organic/polymeric materials, potentially offer low cost, functionalization through molecular design, low volume variation during cycling,<sup>23,24</sup> multiple redox centers, and excellent electrical conductivities and stabilities associated with the delocalization of electrons.<sup>25,26</sup> While similar to  $\pi$ - $\pi$  conjugated materials,  $\pi$ -d structures constructed by the hybridization of the frontier  $\pi$  orbital of the conjugated ligand and the d-orbital of a transition metal, are far less investigated, particularly as sulfur hosts in LSBs.

In this work, we detail the synthesis of a novel one dimensional (1D)  $\pi$ -d conjugated Ni-based MOF (Ni-MOF-1D). We demonstrate the electrons of the Ni-MOF-1D chains to be delocalized forming a large conjugation system, and providing parallel 1D paths for electron conduction and  $\text{Li}^+$  diffusion. We further investigate the electrochemical behavior of this material as sulfur host in LSBs and demonstrate that S@Ni-MOF-1D electrodes deliver a superior rate performance and extraordinary stability. The obtained results are rationalized with the help of density functional theory (DFT) calculations.

## Results and Discussion

Ni-MOF-1D complexes were synthesized by coordinating  $\text{Ni}^{2+}$  with 1,2,4,5-benzenetetramine tetrahydrochloride and the posterior Schiff-based reaction with 1,1,3,3-tetramethoxypropane.

<sup>27</sup> In the final product, each  $\text{Ni}^{2+}$  is coordinated to four N atoms of two 1,2,4,5-benzenetetramine tetrahydrochloride molecules via d- $\pi$  hybridization (**Figure 1a**). Compared with conventional MOFs, the  $\pi$ -d hybridization within Ni-MOF-1D delivers a large density of delocalized electrons that provides a distinctive high electrical conductivity, exceeding even that of activated carbon.<sup>26,28</sup>

Scanning electron microscopy (SEM) analysis showed Ni-MOF-1D to be characterized by a stacked-layered structure (Figure 1b, Figure S1a,b). Energy-dispersive X-ray spectroscopy (EDX) displayed the atomic ratio of Ni, N and C to be *ca.* 1:4:6, consistent with the  $\text{Ni}^{2+}$  bonding to 1,2,4,5-benzenetetramine tetrahydrochloride via its coordination with four N atoms. Aberration-corrected high angle annular dark-field scanning transmission electron microscopy (HAADF-STEM) images coupled with EDX elemental maps (Figure 1c, S1c) showed C, N, and Ni to be homogeneously distributed within Ni-MOF-1D. The presence of oxygen was associated with the solvent used for TEM sample preparation, and with the high affinity of Ni-MOF-1D for trapping oxygen and moisture.<sup>29</sup> X-ray diffraction (XRD) analysis showed the Ni-MOF-1D to present a low crystallinity. Besides, XRD patterns displayed no diffraction peak corresponding to a nickel-based crystal structure, which suggested the absence of Ni-related crystalline nanoparticles or clusters (Figure S1d) and is consistent with HAADF-STEM analysis (Figure S2).

Integrated differential phase-contrast STEM (iDPC-STEM) images at different magnifications showed the Ni-MOF structures to have a 1D morphology (Figure 1d-f, S3). Taking advantage of the sensitivity of iDPC-STEM to the atomic number, higher magnification images showed Ni, with a high atomic number and thus a bright contrast, to be distributed as single atoms within Ni-MOF (Figure 1g).

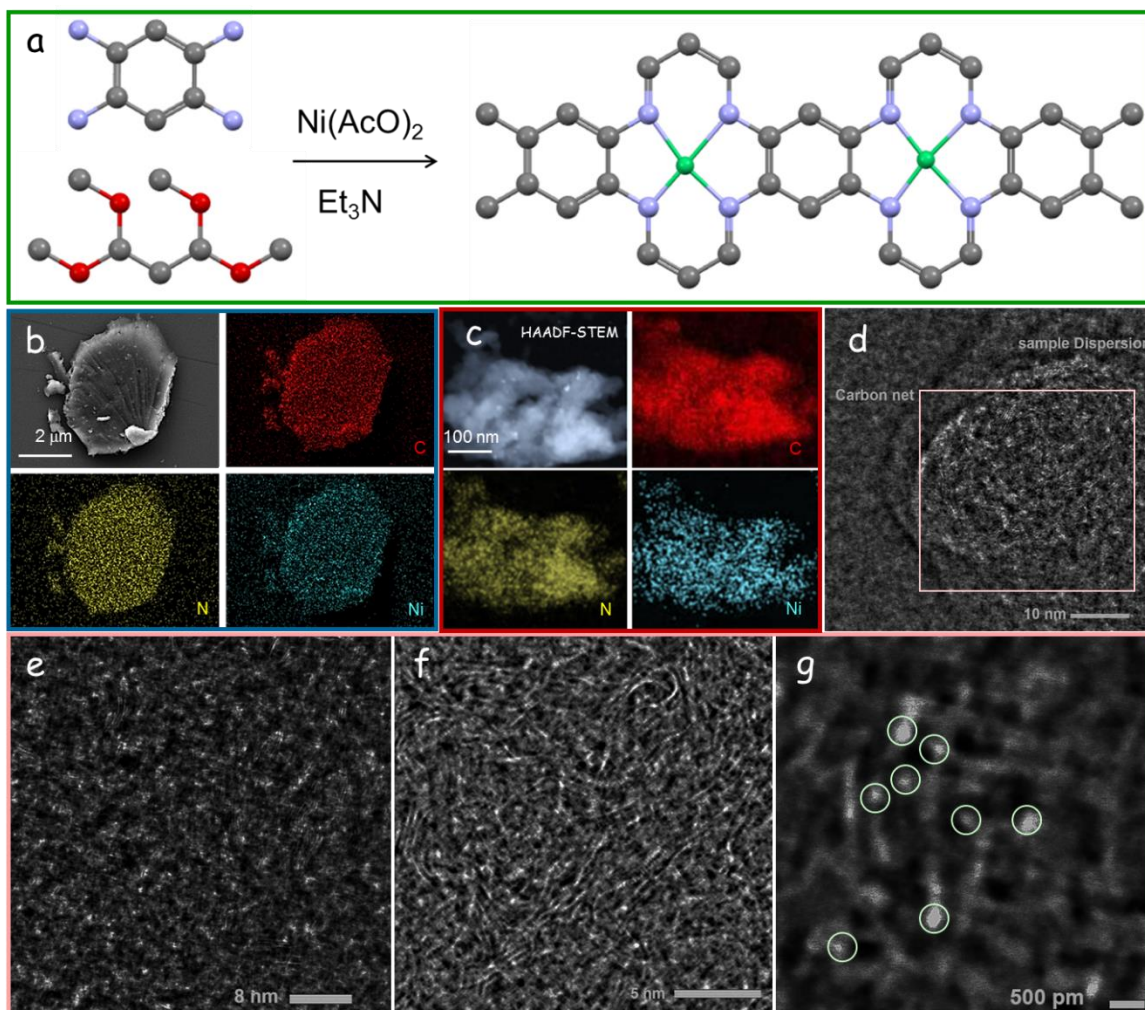


Figure 1. (a) Schematic illustration of the synthesis of Ni-MOF-1D (blue = nitrogen, grey = carbon, red = oxygen, green = nickel). (b) SEM image and SEM-EDX elemental maps of Ni-MOF-1D. (c) STEM-HAADF image and detailed STEM-EDX elemental maps of Ni-MOF-1D. (d-g) iDPC-STEM images at different magnifications of Ni-MOF-1D. Green circles display single Ni atoms shown as bright contrast spots.

X-ray photoelectron spectroscopy (XPS) was used to further analyze the elemental composition and chemical states of Ni-MOF-1D (Figure S4). The high-resolution C 1s XPS spectrum was fitted using four bands, being the main one associated with the C-C bond and used as a reference at 284.6 eV (Figure S4b).<sup>30</sup> The high-resolution N 1s XPS spectrum was fitted with three bands at 398.5 eV, 400.1 eV and 401.5 eV, which correspond to C=N, C-N, H-N bonds, respectively (Figure S4c).<sup>31</sup> In the high-resolution Ni 2p XPS spectrum (Figure S4d), a doublet at 855.6 eV (Ni 2p<sub>3/2</sub>) and 873.3 eV (Ni 2p<sub>1/2</sub>) was assigned to a Ni<sup>x+</sup> chemical environment.<sup>31,32</sup>



The chemical structure of Ni-MOF-1D and particularly the valence state of Ni was more precisely investigated by means of X-ray absorption near-edge structure (XANES) measurements using a Ni foil and NiO as references (Table S1). As shown in **Figure 2a**, the edge structure of Ni-MOF-1D in the XANES spectra is much closer to that of NiO than to Ni, meaning that the valence state of Ni in Ni-MOF-1D is higher than that of the metallic state, consistently with XPS results.<sup>33,34</sup> The absorption edge position of Ni-MOF-1D was consistent with a Ni coordination environment resembling that of Ni-N bond in Ni-MOF-1D. The Fourier transformed extended X-ray absorption fine structure (FT-EXAFS) spectrum of the Ni foil displayed a main peak at 2.23 Å standing for the Ni-Ni bond. For NiO, FT-EXAFS peaks at 1.62 Å and 2.69 Å are associated with Ni-O and Ni-Ni bonds, respectively (Figure 2b).<sup>34,35</sup> The FT-EXAFS spectrum of Ni-MOF-1D displayed a peak at 1.40 Å, which was attributed to a Ni-N bond, further demonstrating the coordination of nickel with nitrogen in Ni-MOF-1D.<sup>36</sup> Figure 2c shows the oscillation curves of Ni-MOF-1D, the Ni foil and NiO in the k range 0-14.0 Å<sup>-1</sup>. Ni-MOF-1D displayed the strongest decrease in signal intensity, pointing towards a higher disorder.

To visualize the coordination environments in both the K and R spaces, a wavelet transform (WT) analysis of the Ni k-edge EXAFS spectrum was carried out (Figure 2d-f, S5). The contour plot of the reference Ni foil exhibited a WT maximum at 7.2 Å<sup>-1</sup>, associated with Ni-Ni. The reference NiO exhibited two WT maxima, at 6.8 Å<sup>-1</sup> and 5.0 Å<sup>-1</sup>, corresponding to Ni-Ni and Ni-O, respectively. Ni-MOF-1D displayed a single WT maximum located at 4.6 Å<sup>-1</sup>, consistent with the Ni-N chemical environment.<sup>35</sup>

The <sup>1</sup>H magnetic angle spinning nuclear magnetic resonance (MAS-NMR) spectrum of Ni-MOF-1D extended 160 ppm to include all the spinning sidebands (SSBs) due to the rigid character of the molecule (Figure S6). To determine the isotropic signal, spectra at 8 kHz and 10 kHz were acquired. The SSBs vary position upon changing spinning rate, while the isotropic peak remains the same. For better clarity, only the isotropic <sup>1</sup>H NMR signal and its simulation are displayed in Figure 2g. The two resonances appearing at -1.1 and -1.3 ppm are assigned to the protons attached to the N/Ni hybrid hexatomic ring and the ones bonded to the aromatic ring in the main chain, respectively. Additionally, the occupancies of the two sorts of protons are 73% and 27%, consistently with the structure. The negative <sup>1</sup>H shifts are mainly attributed

to the shielding from the synergistic effect of Ni atoms and the molecular interaction in space.<sup>37,38</sup> Moreover, the broad unresolved  $^{13}\text{C}$  NMR spectrum, as displayed in Figure 2h, also confirms the hard structure of the material. The central resonances in the range 120 - 160 ppm arise from the aromatic carbons and C=C in the hybrid rings.

The presence of delocalized electrons was further confirmed by continuous-wave electron paramagnetic resonance (CW-EPR) analysis. Ni-MOF-1D displays a narrow and weak EPR resonance at 560 mT which cannot be assigned to Ni but to the delocalized electrons along its double bond (Figure 2i).<sup>39 40</sup>

The electronic band structure of Ni-MOF-1D obtained from the DFT calculations within the HSE06 functional and the corresponding first Brillouin zone are displayed in Figure 2k,l. Several bands cross the Fermi level, demonstrating the metallic nature of Ni-MOF-1D.<sup>26,31</sup>

Figure 2m shows the charge density projected-real space for Ni-MOF-1D. The charge density increases around Ni and decreases in the connected carbon six-membered ring. The charge density projections to the x-axis and y-axis direction are presented in Figure S7. A positive charge density expands along the y-axis direction, i.e. along the Ni-MOF-1D extending direction. On the other hand, in the x-axis the charge density is zero outside of the range 4-13 Å. Thus, charge is more easily transferred along the y-axis than the x-axis.

The electron localization function (ELF) was used to investigate the covalence/iconicity of Ni-MOF-1D (Figure 2n and S8).<sup>41,42</sup> The warmer the color, ELF values closer to 1, the fewer the delocalized electrons, and the weaker the catalytic ability to regulate the adsorbed species. It can be seen that there are delocalized electrons around Ni, which can efficiently regulate the adsorbent, pointing at the Ni center as the catalytic active site.

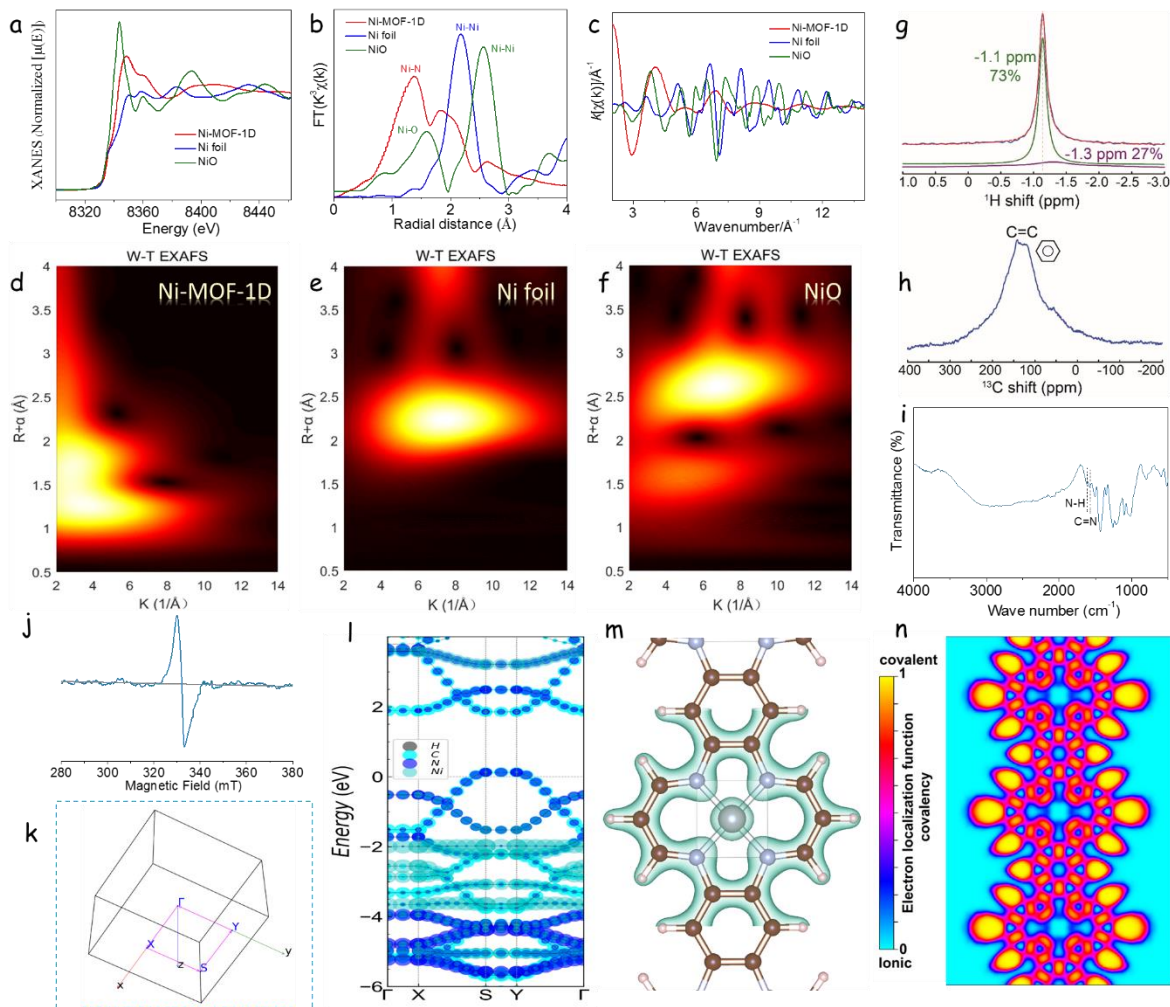


Figure 2. (a) XANES spectra of Ni-MOF-1D, a Ni foil and NiO. (b) Ni K-edge FT-EXAFS spectra in R space of Ni-MOF-1D, Ni foil and NiO. (c) EXAFS oscillations of Ni-MOF-1D with respect to the reference samples. (d-f) Wavelet transform contour plots at Ni K-edge of Ni-MOF-1D, Ni foil, and NiO. (g) Isotropic signal of <sup>1</sup>H NMR spectrum and (h) <sup>13</sup>C MAS-NMR spectrum for Ni-MOF-1D. In (g), the blue curve displays the experimental data and the red-dashed line is the simulation. The position and occupancy are marked next to each resonance. (i) FTIR spectra of Ni-MOF-1D sample. (j) CW-EPR spectrum of Ni-MOF-1D, with g factor of 1.998, being a footprint of delocalized electrons within the polymer. (k) First Brillouin zone, (l) calculated electronic band structure, (m) charge density, and (n) ELF of Ni-MOF-1D.

To evaluate the performance of Ni-MOF-1D as sulfur host in LSBs, sulfur was introduced within the Ni-MOF-1D by a melt-diffusion process. SEM-EDX elemental maps displayed the four elements, S, C, N, and Ni, to be uniformly distributed throughout the composite material

(Figure S9a,b). The XRD pattern of S@Ni-MOF-1D further confirmed the loading of crystalline sulfur (JCPDS No. 65-1101) within S@Ni-MOF-1D composite (Figure S9c).<sup>43</sup> Thermogravimetric analysis (TGA) quantified the sulfur content in the S@Ni-MOF-1D composite at 70.2 wt% (Figure S9d). Besides, the Brunauer–Emmett–Teller (BET) specific surface area of Ni-MOF-1D was  $216.8 \text{ m}^2 \text{ g}^{-1}$ , and it decreased to  $8.6 \text{ m}^2 \text{ g}^{-1}$  with the loading of the porous structure with sulfur (Figure S9e). These results overall illustrate the successful incorporation of sulfur into Ni-MOF-1D.

The four-point probe method was used to determine the electrical conductivities of the host materials before and after sulfur fusion (Figure S10). Ni-MOF-1D exhibited a relatively high electrical conductivity of  $156.7 \text{ S cm}^{-1}$ , well above that of a porous carbon reference (Super P,  $12.5 \text{ S cm}^{-1}$ ). After fusion with sulfur, S@Ni-MOF-1D showed an electrical conductivity up to  $19.1 \text{ S cm}^{-1}$ , nearly fivefold above that of S@Super P ( $3.8 \text{ S cm}^{-1}$ ).

To study the LiPS adsorption ability of the host material, the same amount of Ni-MOF-1D and the Super P carbon reference were immersed in a  $1 \times 10^{-2} \text{ M Li}_2\text{S}_4$  solution. After 12h, the solution containing Super P still displayed the dark yellow color of the initial  $\text{Li}_2\text{S}_4$  solution, while the solution containing Ni-MOF-1D was mostly transparent. This observation was confirmed by the UV–vis spectrum of the solution in the range of 400–500  $\text{nm}$  (**Figure 3a**). Ni-MOF-1D showed the lowest LiPS-related absorbance peaks, indicating the least amount of LiPS residue in the solution. This result demonstrates the strong LiPS adsorption capability of Ni-MOF-1D compared with a conventional carbonaceous support.<sup>44,45</sup>

The high-resolution N 1s and Ni 2p XPS spectra obtained from Ni-MOF-1D before and after  $\text{Li}_2\text{S}_4$  adsorption are displayed in Figures 3b and 3c, respectively. After the  $\text{Li}_2\text{S}_4$  adsorption, the Ni 2p and N 1s peaks showed a significant shift to higher binding energies, which denoted a strong chemical interaction between  $\text{Li}_2\text{S}_4$  and Ni-MOF-1D.<sup>29</sup>

To further evaluate the interaction between LiPS and Ni-MOF-1D, DFT calculations were conducted. Figure S11 and S12 display the optimized adsorption configuration of LiPS species at six different lithiation stages ( $\text{Li}_2\text{S}$ ,  $\text{Li}_2\text{S}_2$ ,  $\text{Li}_2\text{S}_4$ ,  $\text{Li}_2\text{S}_6$ ,  $\text{Li}_2\text{S}_8$  and  $\text{S}_8$ ) on Super P and Ni-MOF-1D. Remarkably, the S and Li atoms of  $\text{Li}_2\text{S}_x$  species can form chemical bonds with Ni and N in Ni-MOF-1D, through the coupling Ni and Li Lewis acids having unoccupied orbitals with S and N Lewis bases having lone electron pairs.<sup>21,45</sup> Taking  $\text{Li}_2\text{S}_4$ -adsorbed structures as

an example (Figure 3d), a binding energy ( $E_b$ ) of -4.59 eV on Ni-MOF-1D was calculated. Figure 3e further displays the  $E_b$  of LiPS species at six different lithiation stages. DFT calculations showed the absolute binding energies for Ni-MOF-1D to be higher than those for the porous carbon used as a reference, Super P. These results suggest robust chemisorption of LiPS species on Ni-MOF-1D, demonstrating its high potential effectiveness to suppress the LiPS shuttle effect.

DFT calculations were further conducted to uncover the redox kinetics of the LiPS conversion. The initial state, transition state and final state of  $\text{Li}_2\text{S}$  decomposition on Ni-MOF-1D and carbon are displayed in Figure S13 and S14. As shown in Figure 3f, the calculated decomposition energy barrier of  $\text{Li}_2\text{S}$  on the surface of the Ni-MOF-1D was just 0.67 eV that was much lower than carbon (2.12 eV). Thus, Ni-MOF-1D could greatly reduce the  $\text{Li}_2\text{S}$  decomposition energy barrier, facilitate delithiation reaction kinetics and enhance the redox reversibility between  $\text{Li}_2\text{S}$  and LiPS in electrochemical process.<sup>35,46</sup>

Besides, the Gibbs free energies for the S reduction pathways of Ni-MOF-1D cathodes were calculated. The overall process of the reversible formation of  $\text{Li}_2\text{S}$  from  $\text{S}_8$  and Li was considered. During the discharge process, the first step involves the double reduction of  $\text{S}_8$  with two  $\text{Li}^+$  to form  $\text{Li}_2\text{S}_8$ , and then  $\text{Li}_2\text{S}_8$  undergoes further reduction, forming three intermediate LiPS;  $\text{Li}_2\text{S}_6$ ,  $\text{Li}_2\text{S}_4$ , and  $\text{Li}_2\text{S}_2$ , producing  $\text{Li}_2\text{S}$  as the final product. The optimized configuration of the intermediates and their Gibbs free energy profiles is shown in Figure 3g. The largest increase of Gibbs free energy was obtained for the conversion from  $\text{Li}_2\text{S}_2$  to  $\text{Li}_2\text{S}$  species, suggesting this step as the rate-limiting for the total discharge process.<sup>29,46</sup> The free energy increase was lower for Ni-MOF-1D (0.75 eV) than for carbon (1.17 eV), suggesting that the reduction of S is more thermodynamically favourable on Ni-MOF-1D than on carbon substrate.

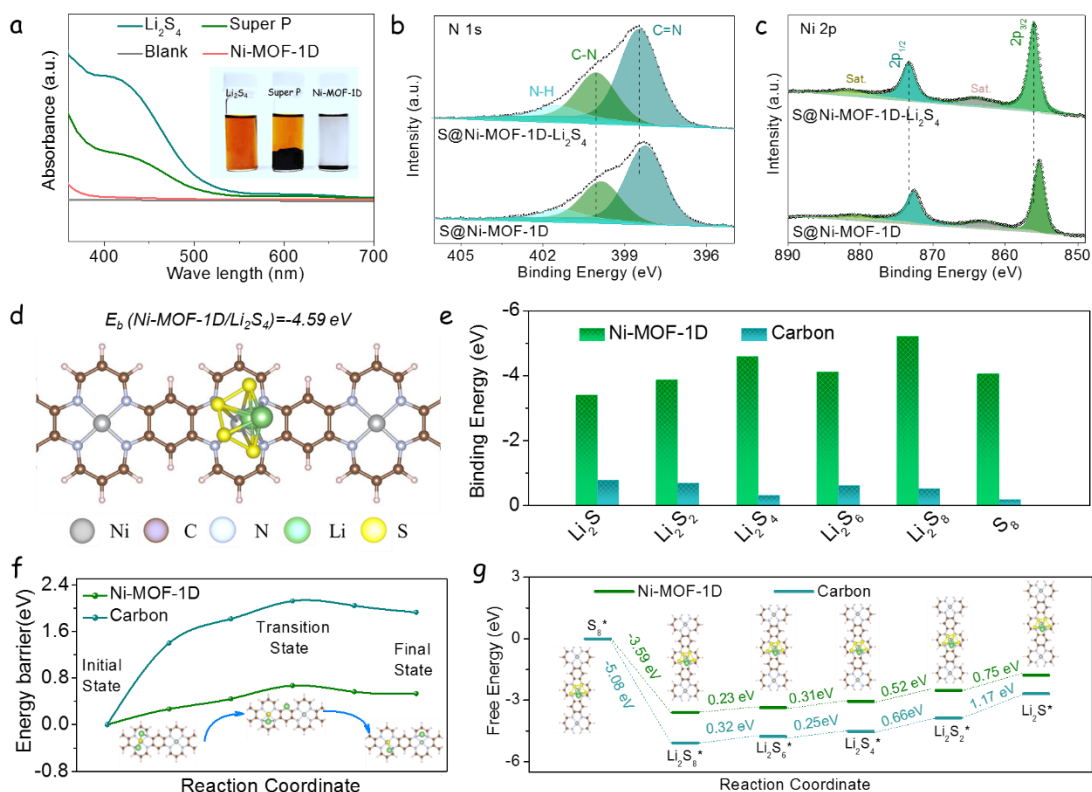


Figure 3. (a) UV–Vis spectra and optical images of the polysulfide solutions after interaction with different adsorbents overnight. (b) High resolution N 1s XPS spectra from Ni-MOF-1D before and after the Li<sub>2</sub>S<sub>4</sub> adsorption test. (c) High resolution Ni 2p XPS spectra of Ni-MOF-1D before and after adsorption of Li<sub>2</sub>S<sub>4</sub>. (d) Relaxed Li<sub>2</sub>S<sub>4</sub>-adsorbed structure on the surface of Ni-MOF-1D calculated with DFT. (e) Binding energies between LiPS species (Li<sub>2</sub>S, Li<sub>2</sub>S<sub>2</sub>, Li<sub>2</sub>S<sub>4</sub>, Li<sub>2</sub>S<sub>6</sub>, Li<sub>2</sub>S<sub>8</sub> and S<sub>8</sub>) and Ni-MOF-1D or carbon as calculated by DFT. (f) Decomposition energy barriers of Li<sub>2</sub>S on Ni-MOF-1D and carbon for different adsorbate configurations. (g) Gibbs free energy profiles and adsorption conformation of LiPS species on Ni-MOF-1D, showing a much lower reaction free energy from Li<sub>2</sub>S<sub>2</sub> to Li<sub>2</sub>S on Ni-MOF-1D than carbon.

To analyze the electrocatalytic activity of Ni-MOF-1D for polysulfide conversion, CV measurements on a symmetric cell were performed within a voltage window of -1.0 to 1.0 V in a 0.5 M Li<sub>2</sub>S<sub>6</sub> and 1 M LiTFSI DOL/DME (v/v = 1/1) electrolyte (**Figure 4a**). Ni-MOF-1D electrodes exhibited a cathodic peak at -0.30 V and an anodic peak at 0.30 V associated with the reaction: <sup>47</sup>



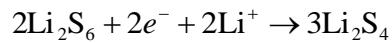
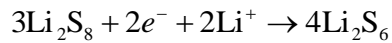
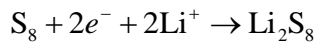
and another cathodic peak at -0.25 V and anodic peak at 0.25 V that correspond to the reaction:



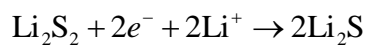
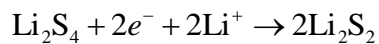
CV curves of symmetric cells with Ni-MOF-1D electrodes displayed significantly higher peak current densities than cells with Super P electrodes. These results demonstrate that Ni-MOF-1D electrodes accelerate the electrochemical reduction and oxidation reaction kinetics of liquid-to-solid ( $\text{Li}_2\text{S} \leftrightarrow \text{S}_6^{2-} \leftrightarrow \text{S}_8$ ) conversion. Besides, approximately rectangular-shaped CV curves were obtained from Ni-MOF-1D electrodes in a  $\text{Li}_2\text{S}_6$ -free electrolyte, suggesting a pure capacitive behavior (Figure S15a).<sup>45,48</sup>

Almost unchanged CV curves were obtained during 50 cycles, pointing toward an excellent stability of the Ni-MOF-1D electrodes (Figure S15b). A similar CV profile was also obtained at different scanning rates from symmetric cells with Ni-MOF-1D electrodes (Figure S15c). Figure S16 shows the electrochemical impedance spectroscopy (EIS) results obtained from Ni-MOF-1D and Super P electrodes, and the simulated equivalent circuit. EIS data shows the Ni-MOF-1D electrodes to be characterized by much lower charge-transfer resistance ( $R_{ct}$ ) than Super P, which points at a significantly faster charge transfer at the Ni-MOF-1D/polysulfide interface than at the Super P/polysulfide interface.<sup>45</sup>

CV measurements using LSB coin cells based on S@Ni-MOF-1D and S@Super P cathodes are presented in Figure 4b. A first cathodic peak (peak I) was identified with the reactions:<sup>49,50</sup>



The second cathodic peak (peak II) accounted for the reactions:



The anodic peak (peak III) corresponded to the reverse oxidation of short-chain sulfides to LiPS and eventually to sulfur.<sup>51</sup> S@Ni-MOF-1D electrodes displayed much higher peak currents and more positive/negative potentials of the cathodic/anodic peaks than S@Super P, demonstrating

the effective role of Ni-MOF-1D in promoting the LiPS catalytic redox reaction (Figure 4b,c). The catalytic activity was quantified through the onset potential at  $10 \mu\text{A cm}^{-2}$  beyond the baseline current (Figure S17, 4c).<sup>29,52</sup> The cells based on S@Ni-MOF-1D electrodes systematically showed higher onset potentials of cathodic peaks (peak I and peak II) and lower onset potentials of the anodic peak (peak III) with respect to cells based on S@Super P, demonstrating faster kinetics of the LiPS redox reaction.

The electrocatalytic activity of Ni-MOF-1D-based electrodes was further analyzed by CV at different scan rates, from 0.1 to 0.5  $\text{mV s}^{-1}$  (Figure 4d). When increasing the scan rate, S@Ni-MOF-1D-based cells exhibited higher redox peak currents and lower polarization potentials compared with S@Super P-based cells (Figure S18). Besides, the CV curves measured from S@Ni-MOF-1D cathodes almost overlap during the first four cycles, demonstrating a good reversibility of the sulfur redox reactions (Figure S19). The cathodic and anodic peak currents showed a linear relationship with the square root of the scanning rate, consistently with a diffusion-limited reaction. Thus, the diffusion constant of lithium ions ( $D_{\text{Li}^+}$ ) was calculated through the classical Randles–Sevcik equation:<sup>53,54</sup>

$$I_p = (2.69 * 10^5) n^{1.5} A D_{\text{Li}^+}^{0.5} C_{\text{Li}^+} \nu^{0.5}$$

Where  $I_p$  is the peak current density,  $n$  is the electron transferred number,  $A$  is the geometric area of the electrode,  $C_{\text{Li}^+}$  is the concentration of  $\text{Li}^+$  in the electrolyte, and  $\nu$  is the scan rate.  $A$ ,  $n$ , and  $C_{\text{Li}^+}$  are constant in this equation, thus sharper  $I_p/\nu^{0.5}$  slopes denote faster  $\text{Li}^+$  diffusion. As displayed in Figure S20, compared with S@Super P, S@Ni-MOF-1D electrodes exhibited the sharpest slopes, pointing towards the highest  $\text{Li}^+$  diffusivity during the redox reactions. In peak I, II and III, S@Ni-MOF-1D electrodes were characterized by a  $D_{\text{Li}^+}$  of  $2.0 \times 10^{-7}$ ,  $3.2 \times 10^{-7}$ , and  $5.2 \times 10^{-7} \text{ cm}^2 \text{ s}^{-1}$ , respectively, significantly above those of S@Super P (Figure 4e). We assigned the higher  $\text{Li}^+$  diffusivities to the relief of the shuttle effect and the outstanding catalytic activity of the Ni-MOF-1D host in accelerating the LiPS conversion kinetics. These properties contributed to preventing the formation of a high viscosity electrolyte through the dissolution of LiPS and the deposition of insulating  $\text{Li}_2\text{S}_2/\text{Li}_2\text{S}$  on the electrode.<sup>48,53</sup>

The galvanostatic charge/discharge profiles for S@Ni-MOF-1D and S@Super P electrodes at a current rate of 0.1 C are displayed in Figure 4f. The charge/discharge curves displayed two discharge plateaus and one charge plateau, which is consistent with CV results and to the



multistep sulfur reaction mechanism. The voltage gap between the second discharge and the charge plateaus was considered as the polarization potential ( $\Delta E$ ).<sup>45,55</sup> S@Ni-MOF-1D electrodes displayed a lower polarization potential ( $\Delta E = 131$  mV) than S@Super P electrodes ( $\Delta E = 208$  mV) (Figure 4g), again consistent with the superior catalytic activity of Ni-MOF-1D to accelerate the conversion of LiPS.

Another quantitative indication of the catalytic activity of the host materials toward the LiPS conversion reaction is the ratio Q2/Q1, where Q1 is the capacity of the first discharge plateau ascribed to the reduction of sulfur to soluble LiPS ( $S_8 + 4Li^+ + 4e^- \rightarrow 2Li_2S_4$ ), and Q2 is the capacity of the second discharge plateaus, corresponding to the subsequent reduction to insoluble sulfide ( $2Li_2S_4 + 12Li^+ + 12e^- \rightarrow 8Li_2S$ ).<sup>56,57</sup> If all soluble LiPS are further reduced to insoluble lithium sulfide, Q2/Q1=3. Thus, host materials with high catalytic activity toward LiPS reduction provide Q2/Q1 ratios close to 3. S@Ni-MOD-1D exhibited an excellent Q2/Q1 = 2.80, well above that of the porous carbon host (S@Super P, Q2/Q1=1.79, Figure 4g).

S@Ni-MOF-1D electrodes also involved a lower overpotential than S@Super P for LiPS reduction to  $Li_2S_2/Li_2S$  and  $Li_2S$  oxidation, as observed in the smaller voltage step at the initial discharging period (Figure 4h),<sup>46</sup> and the smaller voltage dip at the beginning of the initial charging period (Figure S21),<sup>53</sup> respectively.

Potentiostatic nucleation and dissolution experiments were performed to further assess the catalytic effect of the electrode materials on the reversible reaction between polysulfides and  $Li_2S_2/Li_2S$ . As shown from the potentiostatic discharge profiles in Figure 4i, Ni-MOF-1D electrodes exhibit shorter nucleation and growth times, and higher capacity of  $Li_2S$  precipitation ( $303.5$  mA h g<sup>-1</sup>) than Super P electrodes ( $115.6$  mA h g<sup>-1</sup>), as calculated based on Faraday's law. This result further suggests that Ni-MOF-1D significantly lowers the energy barrier of the  $Li_2S$  nucleation, accelerating the  $Li_2S$  precipitation kinetics.<sup>48,58</sup>

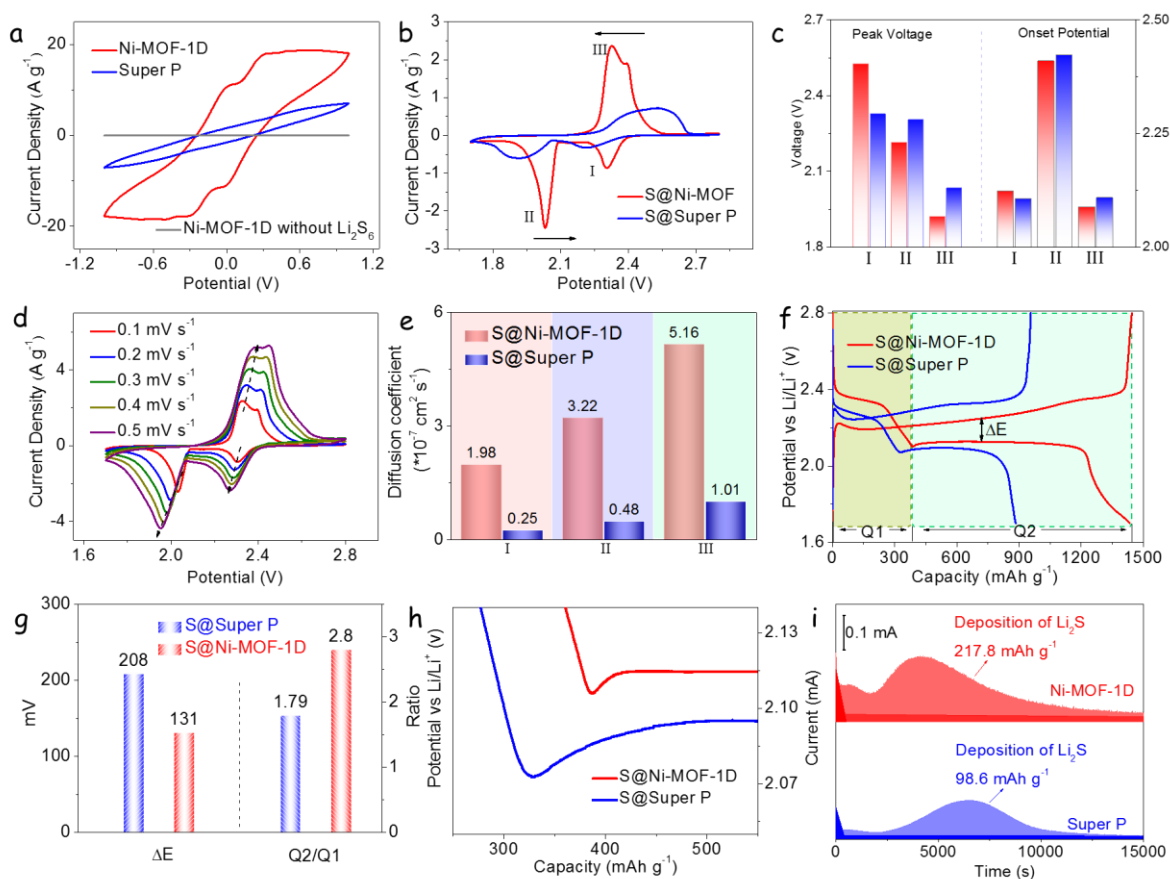


Figure 4. (a) CV profiles of symmetric cells with Ni-MOF-1D and Super P host materials in an electrolyte containing 0.5 mol L<sup>-1</sup> Li<sub>2</sub>S<sub>6</sub> and 1 mol L<sup>-1</sup> LiTFSI dissolved in DOL/DME (v/v = 1/1). (b) CV profiles of Li-S coin cells at a scan rate of 0.1 mV s<sup>-1</sup>. (c) Peak voltages and onset potentials of Li-S cells based on the CV curves. (d) CV profile of the S@Ni-MOF-1D electrode with scan rates range from 0.1-0.5 mV s<sup>-1</sup>. (e) Li<sup>+</sup> diffusion coefficient of S@Ni-MOF-1D and S@Super P electrodes calculated from I, II, and III. (f) Galvanostatic charge/discharge profiles of various electrodes with a 0.1 C current rate. (g) Values of ΔE and Q2/Q1 obtained from charge/discharge profiles. (h) Discharge curves of S@Ni-MOF-1D and S@Super P electrodes exhibiting the overpotentials for the transformation from soluble LiPS to insoluble Li<sub>2</sub>S<sub>2</sub>/Li<sub>2</sub>S. (i) Potentiostatic discharge profile at 2.05 V on S@Ni-MOF-1D and S@Super P electrodes with Li<sub>2</sub>S<sub>8</sub> catholyte to evaluate the nucleation kinetics of Li<sub>2</sub>S.

**Figure 5a** presents the galvanostatic charge/discharge profiles of S@Ni-MOF-1D at different current rates. All discharge curves display two well-defined plateaus, even at the highest current density tested, 8 C. In contrast, S@Super P electrodes showed a high polarization potential and

no capacity response at current rates above 3 C (Figure S22a), due to the large potential barriers and limited conductivity that characterize this electrode material. Figure 5b displays the rate performances of different cells at current rates from 0.1 to 8 C. S@Ni-MOF-1D exhibited a very high initial discharge capacity of 1491 mA h g<sup>-1</sup> at 0.1 C, demonstrating an optimized activity and usage of sulfur. Even at 8 C, the average capacity stabilized at 575 mAh g<sup>-1</sup>. When switched back to 0.2 C, the capacity obtained from the S@Ni-MOF-1D electrode returned to approximately 1150 mAh g<sup>-1</sup>, corresponding to 95.8% of its initial value, pointing toward remarkable reversibility and stability.

The energy conversion efficiency of LSBs in the charging/discharging process was calculated by the ratio of energy output/input:<sup>52,59</sup>

$$E = \int UI dt$$

As shown in Figure 5c, S@Ni-MOF-1D electrodes were characterized by higher energy efficiencies, around 93.0% at 0.1 C than S@Super P (90.8%). Differences in energy efficiency became more notorious when increasing the current rate. At 3C, S@Ni-MOF-1D stabilized the energy efficiency at 87.2%, well above that of S@Super P electrodes (71.3%). We associate these higher energy efficiencies with the lower polarization potentials and better catalytic activity of Ni-MOF-1D.

To evaluate the cycling stability of different host materials, cells based on S@Ni-MOF-1D and S@Super P cathodes were galvanostatically cycled at 1 C (Figure 5d). S@Ni-MOF-1D electrodes enabled an initial capacity of 913 mAh g<sup>-1</sup>, and retained about 94.8% capacity, 869 mAh g<sup>-1</sup>, after 200 cycles. In contrast, S@Super P electrodes displayed a discharge capacity of 408 mAh g<sup>-1</sup> with a capacity retention of 58.3% after 200 cycles. These notable differences might be attributed to the more effective LiPS management and the suppressed shuttle effect achieved by Ni-MOF-1D.

Figure 5e show the Nyquist plot of the EIS data obtained from S@Ni-MOF-1D coin cells before and after cycling at 1 C. The fitting of the data showed S@Ni-MOF-1D electrodes to be characterized by much lower R<sub>ct</sub> compared with S@Super P (Figure S22b), indicating improved electrode kinetics.<sup>60</sup>

Long-cycling tests out of cells based on S@Ni-MOF-1D electrodes were carried out at a higher current rate of 3 C (Figure 5f). After 1000 cycles at 3 C, S@Ni-MOF-1D electrodes still

delivered a discharge capacity of 588 mAh g<sup>-1</sup> with an average 0.018% decay per cycle and a stable and high coulombic efficiency above 99.6%.

The practical application of LSBs requires cathodes providing high energy densities, which involves increasing the sulfur loading. Thus a series of electrochemical tests of S@Ni-MOF-1D electrodes were conducted with a sulfur loading of 4.3 mg cm<sup>-2</sup> (Figure S23). Galvanostatic charge/discharge curves of S@Ni-MOF-1D electrodes showed clear charge/discharge plateaus at the various current rates tested, up to 3C. S@Ni-MOF-1D electrodes delivered a high average initial discharge capacity of 1248 mAh g<sup>-1</sup>, corresponding to an areal capacity of 5.37 mAh cm<sup>-2</sup> (Figure 5g), which is comparable to that of commercial Li-ion batteries (4 mAh cm<sup>-2</sup>). Even at a high current rate of 3 C, S@Ni-MOF-1D electrodes still displayed a discharge capacity of 490 mAh g<sup>-1</sup>, with an areal capacity of 2.11 mAh cm<sup>-2</sup>. This excellent rate performance at a high sulfur loading is attributed to the high electrical conductivity of  $\pi$ -d Ni-based conjugated coordination polymer.

Figure 5h displays the long-term cycling performance of cells based on S@Ni-MOF-1D electrodes with 4.3 mg cm<sup>-2</sup> of sulfur. After 450 cycles, the discharge capacity was maintained at 573 mAh g<sup>-1</sup>, involving an 81.3% capacity retention, *i.e.* a 0.041% average capacity loss per cycle. Besides, S@Ni-MOF-1D electrodes were characterized by a high and stable coulombic efficiency at 99.6%.

Electrochemical results of S@Ni-MOF-1D cathodes for LSBs are compared to other state-of-the-art MOF-based materials in Table S1 (Supporting Information). To illustrate the favorable electrochemical performance of S@Ni-MOF-1D cathodes and the real practical application of related LSBs, one S@Ni-MOF-1D coin cell was used to light up several LED lamps, as observed in the inset of Figure 5h.

Overall, S@Ni-MOF-1D-based cathodes showed an excellent electrochemical performance associated with the following properties: 1) The delocalization of electrons in the  $\pi$ -d system of Ni-MOF-1D provides a superior electrical conductivity, which maximizes the sulfur utilization; 2) The 1D geometry and favorable charge distribution of the Ni-MOF-1D chains provide parallel 1D paths for electron conduction and Li<sup>+</sup> diffusion; and 3) The presence of Ni-N<sub>4</sub> centers, which work as efficient active sites to simultaneously immobilize LiPS and promote

their redox reactions. All these results indicate that S@Ni-MOF-1D electrodes can definitively help LSBs to reach practical applications.

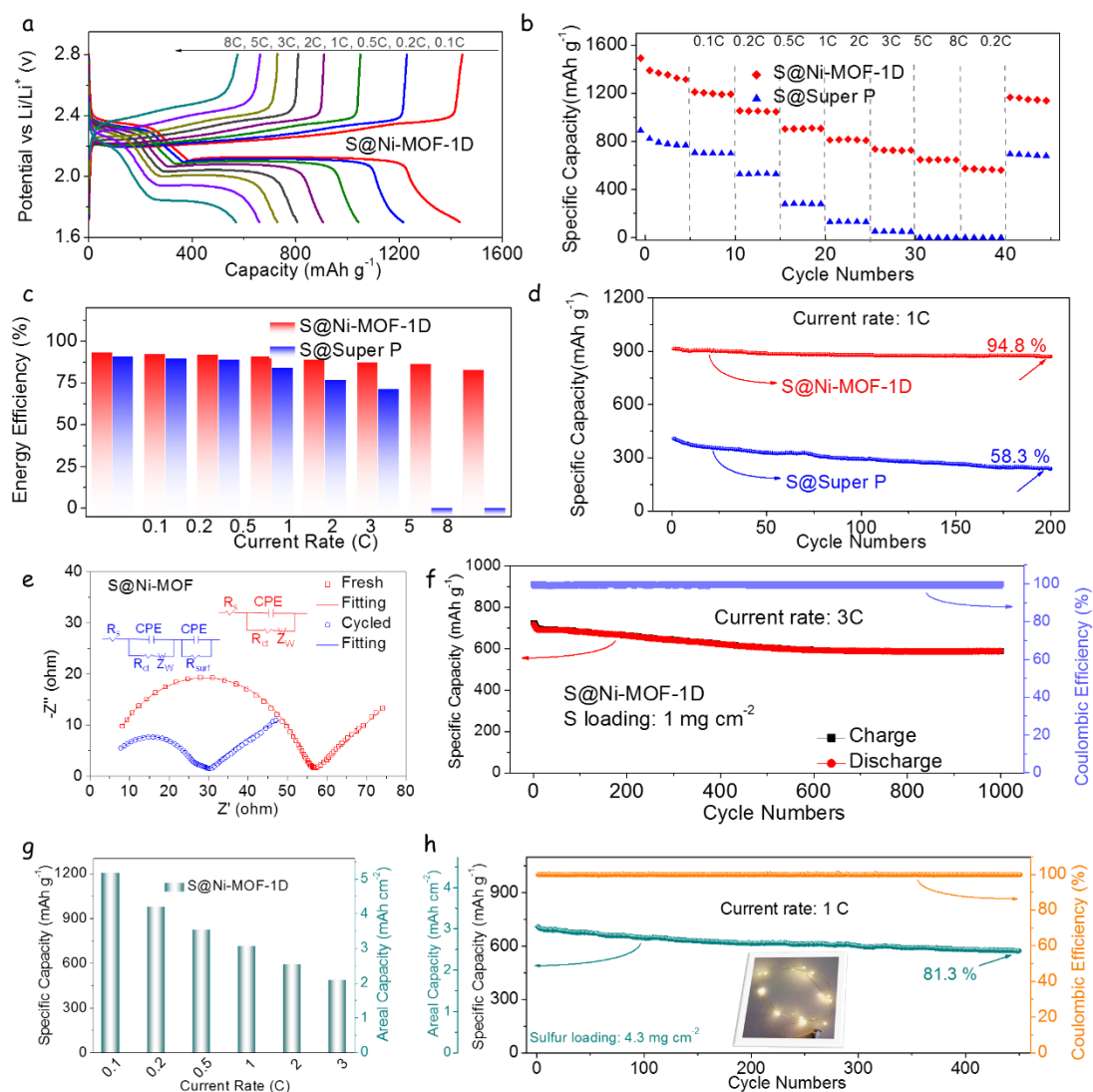


Figure 5. Electrochemical performance of Li-S coin cells. (a) Galvanostatic charge/discharge profile of S@Ni-MOF-1D electrodes at various rates from 0.1 C to 8 C. (b) Rate capabilities of the S@Ni-MOF-1D and S@Super P electrodes at different current rates. (c) Energy efficiency of two different electrodes at various current rates. (d) Capacity retention of S@Ni-MOF-1D and S@Super P electrodes at 1 C over 200 cycles. (e) Nyquist plot of EIS data from S@Ni-MOF-1D electrodes before and after cycling at 1 C. (f) Cycling stability of S@Ni-MOF-1D electrodes at 3 C over 700 cycles. (g) Capacity of S@Ni-MOF-1D electrodes with a 4.3  $\text{mg cm}^{-2}$  sulfur loading. (h) Capacity retention of S@Ni-MOF-1D electrodes with a high sulfur loading of 4.3  $\text{mg cm}^{-2}$ . Inset shows the digital photograph of LED lamps powered by one S@Ni-MOF-1D Li-S coin cell.

## Conclusion

In summary, a high conductivity 1D Ni-MOF was rationally designed, engineered, characterized, and tested as an efficient sulfur host for LSBs. Within this material, a  $\pi$ -d hybridization enables the delocalization of a high density of electrons, which provides a metallic character. The associated high electrical conductivity of Ni-MOF-1D allows overcoming the insulating nature of S,  $\text{Li}_2\text{S}$  and most polar S-based electrodes. Besides, the dissolution of LiPS into the electrolyte is largely prevented by the strong interaction between Ni-MOF-1D and LiPS. In addition, within this structure, the Ni-N coordination centers serve as a bifunctional electrocatalyst to facilitate both the formation and the decomposition of  $\text{Li}_2\text{S}$  during discharge and charge processes, respectively. As a result, S@Ni-MOF-1D delivered impressive rate performance with  $575 \text{ mAh g}^{-1}$  at 8 C, and excellent long-term cycling stability with a minor capacity decay of 0.018% per cycle over 1000 cycles at 3 C. Even at a high sulfur loading of  $4.3 \text{ mg cm}^{-2}$ , S@Ni-MOF-1D cathodes deliver a remarkable areal capacity of  $5.36 \text{ mAh cm}^{-2}$  that can meet the needs of commercial LIBs ( $4 \text{ mAh cm}^{-2}$ ). This work demonstrated Ni-MOF-1D as an excellent sulfur host, acting as multifunctional polysulfide regulators to chemically adsorb LiPS, accelerate  $\text{Li}^+$  diffusion, and catalyze the LiPS conversion reactions. More generally, this work presented new insights and deepen understanding of  $\pi$ -d conjugated MOFs and demonstrated their potential as cathode host material in LSBs.

## Acknowledgements

This work was supported by the European Regional Development Funds and by the Spanish Ministerio de Economía y Competitividad through the projects ENE2016- 77798-C4-3-R, and ENE2017-85087-C3. D. Yang and C. Zhang thank the China Scholarship Council for the scholarship support. Z. Liang acknowledges funding from MINECO SO FPI PhD grant (SEV-2013-0295-17-1). Dr. J. Li obtained International Postdoctoral Exchange Fellowship Program (Talent-Introduction program) in 2019 and is grateful for the project (2019M663468) funded by the China Postdoctoral Science Foundation. Authors acknowledge funding from Generalitat de Catalunya 2017 SGR 327 and 2017 SGR 1246. ICN2 acknowledges the support from the

Severo Ochoa Programme (MINECO, grant no. SEV-2017-0706) and is funded by the CERCA Programme/Generalitat de Catalunya. J. Llorca is a Serra Hünter Fellow and is grateful to MICINN/FEDER RTI2018-093996-B-C31, GC 2017 SGR 128 and to ICREA Academia program.

## References

1. P. G. Bruce, S. A. Freunberger, L. J. Hardwick and J. M. Tarascon, *Nat. Mater.*, 2011, **11**, 19-29.
2. G. Zhou, D.-W. Wang, F. Li, P.-X. Hou, L. Yin, C. Liu, G. Q. Lu, I. R. Gentle and H.-M. Cheng, *Energy Environ. Sci.*, 2012, **5**, 8901.
3. Z. Li, B. Y. Guan, J. Zhang and X. W. Lou, *Joule*, 2017, **1**, 576-587.
4. Z. Xiao, Z. Yang, L. Wang, H. Nie, M. Zhong, Q. Lai, X. Xu, L. Zhang and S. Huang, *Adv. Mater.*, 2015, **27**, 2891-2898.
5. X. Chen, H.-J. Peng, R. Zhang, T.-Z. Hou, J.-Q. Huang, B. Li and Q. Zhang, *ACS Energy Letters*, 2017, **2**, 795-801.
6. Y. Yang, G. Zheng and Y. Cui, *Chem.Soc.Rev.*, 2013, **42**, 3018-3032.
7. X. Liang, Y. Rangom, C. Y. Kwok, Q. Pang and L. F. Nazar, *Adv. Mater.*, 2017, **29**, 1603040.
8. A. Shyamsunder, W. Beichel, P. Klose, Q. Pang, H. Scherer, A. Hoffmann, G. K. Murphy, I. Krossing and L. F. Nazar, *Angew. Chem., Int. Ed.*, 2017, **56**, 6192-6197.
9. Z. Sun, J. Zhang, L. Yin, G. Hu, R. Fang, H. M. Cheng and F. Li, *Nat. Commun.*, 2017, **8**, 14627.
10. J. Xie, B. Q. Li, H. J. Peng, Y. W. Song, M. Zhao, X. Chen, Q. Zhang and J. Q. Huang, *Adv. Mater.*, 2019, **31**, e1903813.
11. L. Ji, M. Rao, S. Aloni, L. Wang, E. J. Cairns and Y. Zhang, *Energy Environ. Sci.*, 2011, **4**, 5053.
12. Z. Li, J. Zhang, B. Guan, D. Wang, L. M. Liu and X. W. Lou, *Nat. Commun.*, 2016, **7**, 13065.
13. C. Zu and A. Manthiram, *Adv. Energy Mater.*, 2013, **3**, 1008-1012.
14. J. Zhang, Z. Li, Y. Chen, S. Gao and X. W. D. Lou, *Angew. Chem. Int. Ed.*, 2018, **130**,

- 11110-11114.
15. Y. Zhong, D. Chao, S. Deng, J. Zhan, R. Fang, Y. Xia, Y. Wang, X. Wang, X. Xia and J. Tu, *Adv. Funct. Mater.*, 2018, **28**, 1706391.
  16. Z. Cheng, Z. Xiao, H. Pan, S. Wang and R. Wang, *Adv. Energy Mater.*, 2018, **8**, 1702337.
  17. D. Cai, B. Liu, D. Zhu, D. Chen, M. Lu, J. Cao, Y. Wang, W. Huang, Y. Shao, H. Tu and W. Han, *Adv. Energy Mater.*, 2020, **10**, 1904273.
  18. Z. Ye, Y. Jiang, L. Li, F. Wu and R. Chen, *Adv. Mater.*, 2020, **32**, e2002168.
  19. S. Bai, X. Liu, K. Zhu, S. Wu and H. Zhou, *Nat. Energy.*, 2016, **1**, 16094.
  20. M. Rana, H. A. Al-Fayaad, B. Luo, T. Lin, L. Ran, J. K. Clegg, I. Gentle and R. Knibbe, *Nano Energy*, 2020, **75**, 105009.
  21. J. Zheng, J. Tian, D. Wu, M. Gu, W. Xu, C. Wang, F. Gao, M. H. Engelhard, J. G. Zhang, J. Liu and J. Xiao, *Nano Lett.*, 2014, **14**, 2345-2352.
  22. Z. Wang, B. Wang, Y. Yang, Y. Cui, Z. Wang, B. Chen and G. Qian, *ACS Appl. Mater. Interfaces*, 2015, **7**, 20999-21004.
  23. D. Cai, M. Lu, Li, J. Cao, D. Chen, H. Tu, J. Li and W. Han, *Small*, 2019, **15**, e1902605.
  24. M. Tang, S. Zhu, Z. Liu, C. Jiang, Y. Wu, H. Li, B. Wang, E. Wang, J. Ma and C. Wang, *Chem*, 2018, **4**, 2600-2614.
  25. V. Rubio-Gimenez, M. Galbiati, J. Castells-Gil, N. Almora-Barrios, J. Navarro-Sanchez, G. Escorcia-Ariza, M. Mattera, T. Arnold, J. Rawle, S. Tatay, E. Coronado and C. Marti-Gastaldo, *Adv. Mater.*, 2018, **30**, 1704291.
  26. J. H. Dou, L. Sun, Y. Ge, W. Li, C. H. Hendon, J. Li, S. Gul, J. Yano, E. A. Stach and M. Dinca, *J. Am. Chem. Soc.*, 2017, **139**, 13608-13611.
  27. J. L. Segura, M. J. Mancheno and F. Zamora, *Chem.Soc.Rev.*, 2016, **45**, 5635-5671.
  28. D. Xing, Y. Wang, P. Zhou, Y. Liu, Z. Wang, P. Wang, Z. Zheng, H. Cheng, Y. Dai and B. Huang, *Appl. Catal., B* 2020, **278**, 119295.
  29. Z. Liang, D. Yang, P. Tang, C. Zhang, J. Jacas Biendicho, Y. Zhang, J. Llorca, X. Wang, J. Li, M. Heggen, J. David, R. E. Dunin - Borkowski, Y. Zhou, J. R. Morante, A. Cabot and J. Arbiol, *Adv. Energy Mater.*, 2020, **11**, 2003507.
  30. X. Hao, Z. Cui, J. Zhou, Y. Wang, Y. Hu, Y. Wang and Z. Zou, *Nano Energy*, 2018, **52**, 105-116.



31. L. Wang, Y. Ni, X. Hou, L. Chen, F. Li and J. Chen, *Angew. Chem., Int. Ed.*, 2020, **59**, 22126-22131.
32. G. Cai, P. Cui, W. Shi, S. Morris, S. N. Lou, J. Chen, J. H. Ciou, V. K. Paidi, K. S. Lee, S. Li and P. S. Lee, *Adv. Sci.*, 2020, **7**, 1903109.
33. X. Xiong, C. Mao, Z. Yang, Q. Zhang, G. I. N. Waterhouse, L. Gu and T. Zhang, *Adv. Energy Mater.*, 2020, **10**, 2002928.
34. K. Jiang, S. Siahrostami, T. Zheng, Y. Hu, S. Hwang, E. Stavitski, Y. Peng, J. Dynes, M. Gangisetty, D. Su, K. Attenkofer and H. Wang, *Energy Environ. Sci.*, 2018, **11**, 893-903.
35. L. Zhang, D. Liu, Z. Muhammad, F. Wan, W. Xie, Y. Wang, L. Song, Z. Niu and J. Chen, *Adv. Mater.*, 2019, **31**, e1903955.
36. C. Zhao, X. Dai, T. Yao, W. Chen, X. Wang, J. Wang, J. Yang, S. Wei, Y. Wu and Yadong Li, *J. Am. Chem. Soc.*, 2017, **139**, 8078–8081.
37. A. Frank, A. Berkefeld, M. Drexler, H. M. Möller and T. E. Exner, *Int. J. Quantum Chem.*, 2013, **113**, 1787-1793.
38. S. A. Rouf, V. B. Jakobsen, J. Mares, N. D. Jensen, C. J. McKenzie, J. Vaara and U. G. Nielsen, *Solid State Nucl. Magn. Reson.*, 2017, **87**, 29-37.
39. A. Ishitani and S. Nagakura, *Mol. Phys.*, 1967, **12**, 1-12.
40. A. N. Ponomaryov, N. Kim, J. Hwang, H. Nojiri, J. van Tol, A. Ozarowski, J. Park, Z. Jang, B. Suh, S. Yoon and K. Y. Choi, *Chem. Asian J.*, 2013, **8**, 1152-1159.
41. Z. Zhao, T. Yu, S. Zhang, H. Xu, G. Yang and Y. Liu, *J. Mater. Chem. A.*, 2019, **7**, 405-411.
42. J. P. Piquemal, J. Pilmé, O. Parisel, H. Gérard, I. Fourré, J. Bergès, C. Gourlaouen, A. De La Lande, M. C. Van Severen and B. Silvi, *Int. J. Quantum Chem.*, 2008, **108**, 1951-1969.
43. M. Xue, Y. Zhou, J. Geng, P. Zeng, Y. Xu, Y. Wang, W. Tang, P. Wu, S. Wei and Yiming Zhou, *RSC Adv.*, 2016, **6**, 91179-91184.
44. T. Lei, W. Chen, J. Huang, C. Yan, H. Sun, C. Wang, W. Zhang, Y. Li and J. Xiong, *Adv. Energy Mater.*, 2017, **7**, 1601843.
45. D. Yang, C. Zhang, J. J. Biendicho, X. Han, Z. Liang, R. Du, M. Li, J. Li, J. Arbiol, J. Llorca, Y. Zhou, J. R. Morante and A. Cabot, *ACS Nano* 2020, **14**, 15492-15504.

46. Z. Du, X. Chen, W. Hu, C. Chuang, S. Xie, A. Hu, W. Yan, X. Kong, X. Wu, H. Ji and L. J. Wan, *J. Am. Chem. Soc.*, 2019, **141**, 3977-3985.
47. H. Lin, L. Yang, X. Jiang, G. Li, T. Zhang, Q. Yao, G. W. Zheng and J. Y. Lee, *Energy Environ. Sci.*, 2017, **10**, 1476-1486.
48. C. Zhang, R. Du, J. J. Biendicho, M. Yi, K. Xiao, D. Yang, T. Zhang, X. Wang, J. Arbiol, J. Llorca, Y. Zhou, J. R. Morante and A. Cabot, *Adv. Energy Mater.*, 2021, **11**, 2100432.
49. S. S. Zhang, *J. Power Sources*, 2013, **231**, 153-162.
50. D. Moy, A. Manivannan and S. R. Narayanan, *J. Electrochem. Soc.*, 2014, **162**, A1-A7.
51. Y. Tian, G. Li, Y. Zhang, D. Luo, X. Wang, Y. Zhao, H. Liu, P. Ji, X. Du, J. Li and Z. Chen, *Adv. Mater.*, 2020, **32**, e1904876.
52. Z. Yuan, H. J. Peng, T. Z. Hou, J. Q. Huang, C. M. Chen, D. W. Wang, X. B. Cheng, F. Wei and Q. Zhang, *Nano Lett.*, 2016, **16**, 519-527.
53. G. Zhou, H. Tian, Y. Jin, X. Tao, B. Liu, R. Zhang, Z. W. Seh, D. Zhuo, Y. Liu, J. Sun, J. Zhao, C. Zu, D. S. Wu, Q. Zhang and Y. Cui, *Proc. Natl. Acad. Sci. USA*, 2017, **114**, 840-845.
54. X. Zhu, W. Zhao, Y. Song, Q. Li, F. Ding, J. Sun, L. Zhang and Z. Liu, *Adv. Energy Mater.*, 2018, **8**, 1800201.
55. S. Niu, S.-W. Zhang, R. Shi, J. Wang, W. Wang, X. Chen, Z. Zhang, J. Miao, A. Amini, Y. Zhao and C. Cheng, *Energy Storage Mater.*, 2020, **33**, 73-81.
56. D. Su, M. Cortie, H. Fan and G. Wang, *Adv. Mater.*, 2017, **29**, 1700587.
57. J. Zhou, R. Li, X. Fan, Y. Chen, R. Han, W. Li, J. Zheng, B. Wang and X. Li, *Energy Environ. Sci.*, 2014, **7**, 2715-2724.
58. F. Y. Fan, W. C. Carter and Y. M. Chiang, *Adv. Mater.*, 2015, **27**, 5203-5209.
59. A. Eftekhari, *Sustainable Energy Fuels*, 2017, **1**, 2053-2060.
60. T. Zhou, W. Lv, J. Li, G. Zhou, Y. Zhao, S. Fan, B. Liu, B. Li, F. Kang and Q.-H. Yang, *Energy Environ. Sci.*, 2017, **10**, 1694-1703.